Low-energy in-line electron holographic imaging of vitreous ice-embedded small biomolecules using a modified scanning electron microscope

Martin Cheung[1*†], Hidehito Adaniya[1†], Cathal Cassidy[1], Masao Yamashita[1] and Tsumoru Shintake[1]

[1]Quantum Wave Microscopy Unit, Okinawa Institute of Science and Technology Graduate University, Kunigami District, Okinawa Prefecture, Japan, 904-0412

*Correspondence: martin.cheung@oist.jp †These authors contributed equally to this work

Key words: scanning electron microscopy, scanning transmission electron microscopy; transmission electron microscopy; in-line electron holography; low-energy; cryo-electron microscopy; vitreous ice; sample preparation; vitrification

Abstract

Cryo-electron microscopy (cryo-EM) has become the method of choice in the field of structural biology, owing to its unique ability to deduce structures of vitreous ice-embedded, hydrated biomolecules over a wide range of structural resolutions. As cryo-transmission electron microscopes (cryo-TEM) become increasingly specialised for high, near-atomic resolution studies, operational complexity and associated costs serve as significant barriers to widespread usability and adoptability. To facilitate the expansion and accessibility of the cryo-EM method, an efficient, user-friendly means of imaging vitreous ice-embedded biomolecules has been called for. In this study, we present a solution to this issue by integrating cryo-EM capabilities into a commercial scanning electron microscope (SEM). Utilising the principle of low-energy in-line electron holography, our newly developed hybrid microscope permits low-to-moderate resolution imaging of vitreous ice-embedded biomolecules without the need for any form of sample staining or chemical fixation. Operating at 20 kV, the microscope takes advantage of the ease-of-use of SEM-based imaging and phase contrast imaging of low-energy electron holography. This study represents the first reported successful application of low-energy in-line electron holographic imaging to vitreous ice-embedded small biomolecules, the effectiveness of which is demonstrated here with three morphologically distinct specimens.

Main text

The field of cryo-electron microscopy (cryo-EM) has seen tremendous technological advancement over the past few decades, pushing achievable structural resolution of biomolecule imaging to levels approaching and even rivalling X-ray crystallography, the gold standard of structural biology (1). In particular, by applying the single-particle EM method, in which electron micrographs of purified biomolecules embedded in suitably thin vitreous (amorphous) ice films (typically <100 nm), structural information of specimens in hydrated, near-physiological states can now be obtained at unprecedented levels of clarity. However, as highlighted by Vinothkumar and Henderson (2016) (2), this unrelenting progress has come at the expense of affordability and accessibility; the prohibitively large costs associated with acquiring and running a high-end cryo-transmission electron microscope (cryo-TEM) facility and steep learning curve for even basic operational competency serve as significant barriers to widespread usability, especially for nonexpert users. Furthermore, while structures visualised at near-atomic resolutions (<5 Å) can reveal intimate biophysical information, structures determined to low-to-moderate resolutions (>5 Å) can still provide important secondary-to-quaternary structural and conformational information and even mechanistic insights. For such studies, the capabilities of high-end, high-resolution cryo-TEMs are often superfluous to the user's requirements.

There have been calls for an alternative means of imaging ice-embedded small biomolecules in order to alleviate the aforementioned issues. While high-resolution imaging would still require high-end cryo-TEMs, a "diagnostic" microscope capable of low-to-moderate cryo-EM imaging would be perfectly suited for sample pre-screening (2). For example, for certain biomolecules, low-to-moderate image resolution would be sufficient to assess important specimen properties such as homo/heterogeneity, structural integrity, and domain flexibility etc., all of which could provide invaluable information to the researcher. Such a microscope could also be used for cryo-EM sample preparation optimisation by providing an efficient means of assessing cryo-sample preparation-related factors such as particle concentration and dispersion, ice thickness, crystalline ice contamination etc., prior to high-

resolution studies. A user-friendly microscope that could fulfil these requirements has the potential to facilitate the expansion of the cryo-EM field by reducing issues of usability and affordability, allowing even nonexpert users to conduct cryo-EM studies and widening the scope of applicability.

A proposed solution to this issue is the adaptation of an existing, more affordable and user-friendly technology to serve this purpose: scanning electron microscopes (SEM). While cryo-TEMs have superior bio-imaging capabilities and versatility compared with SEMs, low-to-moderate resolution image acquisition in SEM can be conducted with relative ease, requiring only a basic understanding of operational procedures in order to achieve satisfactory image quality. Furthermore, the costs associated with running a commercial SEM (e.g. acquisition and maintenance costs) are considerably lower than an equivalent specification TEM (3). Despite the potential of SEM-based microscopes to fulfil this role, technical challenges associated with the low-energy electron beams typically found in commercial SEMs (≤ 30 kV) have hindered the adaptation of this technology for small biomolecule cryo-EM imaging purposes (personal communication with Hitachi High-Technologies, Japan).

Here we present a significant step towards the integration of SEMs into the field of small biomolecule cryo-EM. Based on a commercially available Hitachi SEM platform, our newly developed hybrid microscope (hereinafter referred to as DMF4000; **d**iffraction **m**icroscope with **f**ocused ion beam **4000**) can perform phase contrast imaging via the principle of divergent beam low-energy in-line electron holography (Figure 1.) (4). Dennis Gabor invented in-line electron holography as a means to overcome the then seemingly insurmountable aberration issues associated with conventional TEM optics. By recording the hologram formed by the interference between reference and object (specimen) exit wavefronts, structural phase and amplitude information about the object can be reconstructed by means of mathematical back propagation (5). Pioneering work in this field has previously been reported by Hans-Werner Fink and colleagues who, using a custom built low-energy electron microscope, were able to record electron holograms of individual biomolecules adsorbed to graphene support films (6–11). While studies of this

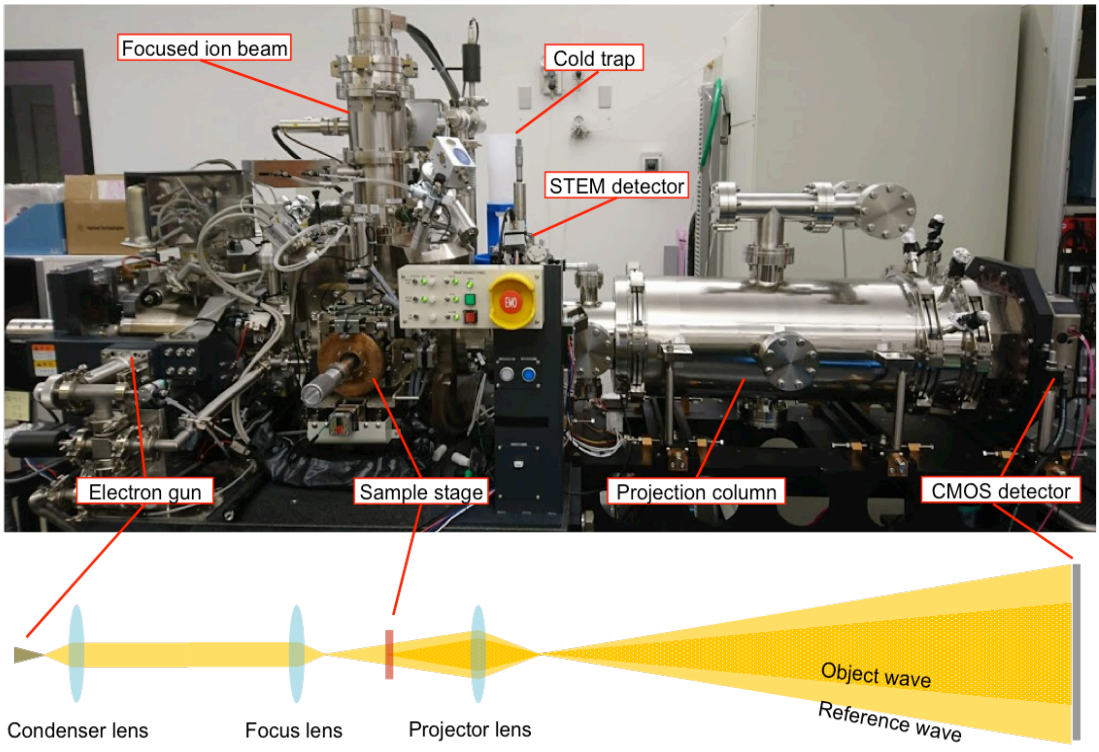

Figure 1. Key mechanical components of DMF4000. (Top) Modifications implemented for the purpose of low-energy in-line electron holographic imaging of samples at cryogenic temperatures include a side-entry holder-compatible sample stage, cold trap, projection column, and complementary metal-oxide-semiconductor (CMOS) detector. (Bottom) Electron beam trajectory from electron gun to CMOS detector. Atypically, electron beam trajectory is parallel to the ground (from left to right).

nature have demonstrated the feasibility of this approach, imaged biomolecules were not hydrated or ice-embedded and therefore did not represent native physiological states. It has been asserted that electron holography, especially at low electron energy regimes, is ill-suited for the imaging of samples prepared by the plunge-freezing method due to deleterious electrostatic charging of the ice film and poor image signal-to-noise ratios (SNR), a consequence of pronounced inelastic scattering (12–14). Despite this, Matsumoto et al., (1995) (15) successfully imaged ice-embedded DNA molecules by in-line electron holography using a Hitachi HF-2000 TEM operating at 100 kV. However, while in-line holograms can be recorded in conventional TEMs by image defocusing, the relatively high electron energies used in such microscopes (between 100–300 kV) do not

permit high-contrast phase imaging of small biomolecules, especially those embedded in vitreous ice films. In this study, we have surmounted various technical hurdles to successfully apply this technology to the imaging of vitreous ice-embedded small biomolecules using a modified commercial SEM operating at 20 kV, without the need for any form of sample staining or chemical fixation thus allowing for true imaging of specimens in near physiological states. By adapting a commercial SEM to record low-energy electron in-line electron cryo-holograms, we demonstrate not only the ability of this imaging method to generate images of vitreous ice-embedded small biomolecules at sufficiently high contrast and clarity to permit sample analysis at nanometer resolution but also the ease with which the technology presented herein could be adapted to other commercially available SEMs.

Methods

Biomolecule purification

Please see supplementary materials

Cryo-sample preparation and loading into DMF4000 Owing to the high ambient humidity in the locality of the experiment (average annual relative humidity ~76%), extra care was taken during sample preparation to minimise exposure to ambient conditions. Vitrification and grid transfer stages of the sample preparation workflow were conducted in a dedicated cryo-EM sample preparation room with humidity controlled to ~30% (Figure S3). In order to reduce crystalline ice contamination arising from ambient moisture, all equipment was thoroughly dried with N_2 before commencing sample preparation.

DMF4000 has a modified sample stage to accommodate side-entry cryo-holders. Due to DMF4000's horizontal orientation (electron beam trajectory is parallel to the ground), we primarily used a Gatan 914 high-tilt cryo-transfer tomography holder to minimise LN_2 spillage during transfer into the microscope and imaging (Figure 1). The associated cryo-workstation was housed within a customised glove box (AS ONE, AS-800P) with constant N_2 flow to generate a positive-pressure, low-humidity environment around the

cryo-workstation (Figure S3). Prior to commencement of sample preparation, the glove box was purged with N_2 to remove any trapped moisture and to reduce the humidity within the glove box to below a few percent (typically below 1%), as measured by a hydro-thermometer (ThermoPORT, TP-200HG).

Plunge-frozen sample grids were prepared using Mark IV FEI Vitrobot and the two-sided blotting, hydrated-graphene oxide process as detailed in Cheung et al., (2018) (16). In general, the precise type of grid used was not found to greatly impact resulting holograms; for consistency, all samples were prepared with R3.5/1 Au 200 mesh grids (Quantifoil). Grid boxes containing ethane plunge-frozen grids were promptly transferred into the glove box and then into cryo-workstation chamber. Despite the low-humidity environment surrounding the cryo-workstation, grid transfer was conducted judiciously to minimise water contamination from entering the cryo-workstation chamber. Where possible, the cryo-workstation chamber cover was kept closed at all times.

To transfer the cryo-holder into the microscope with minimal ice contamination, the cryo-workstation and holder were transferred into an N_2-filled container before being moved to the vicinity of the microscope, followed by immediate insertion into DMF4000.

SEM/STEM imaging and transition to holography mode Full details of DMF4000 technical specifications and operational procedures can be found in Adaniya et al., (2018) (4). After holder insertion into the microscope main chamber, the chamber pressure was allowed to stabilise and reach the normal operating vacuum level of 2.2–2.5 $\times$ 10^{-5} Pa. For the duration of the imaging session, the temperature of the cryo-holder tip was constantly monitored, with imaging only conducted when the measured temperature was around -175 °C. In order to assess the overall quality of the sample grid a low-magnification, 4,000 µm field-of-view (FOV), near-full grid image was acquired in either SEM or bright field-scanning transmission electron microscopy (BF-STEM) mode, with the latter allowing assessment on the general thickness of

the ice film across the grid and the identification of regions suitable for data collection. Suitable areas for imaging were identified and logged.

SEM/STEM probe was brought to point convergence on the carbon film surface by focusing on a surface-located feature within the grid square to the imaged. The position of the stage at this point was designated as *Z*=0 (eucentric height). A full grid square image (FOV, 100 µm) was captured in BF-STEM mode to allow for positions of holes to be identified. To transition from SEM/STEM modes to in-line electron holographic imaging mode, the specimen stage was mechanically shifted 200 µm downstream from point focus. For image acquisition, the BF-STEM detector was retracted off the beam path and electron detection switched to an 8,000 × 8,000 pixel complementary metal-oxide-semiconductor (CMOS) detector (TVIPS) located ~1.4 m downstream from the specimen stage. Pre-activated magnetic steering coils and projection lenses located in the projection column allow holograms to be adjusted to fit the determined detector region and for magnification purposes. Holograms were acquired with a single exposure shot of 200 ms, at a dose rate of ~1 e^-/ $Å^2$/s.

Image reconstruction Phase and amplitude channels were reconstructed by computationally back-propagating recorded holograms to the object plane based on the Fresnel-Kirchhoff diffraction formula. To establish the correct back propagation distances, reference samples of vitreous ice-embedded 30 nm gold particles were prepared using water-diluted solutions of gold nanospheres (nanoComposix, BioPure) and imaged at varying stage offset positions. The clearly definable edges of the gold particles allowed us to visually determine the optimal back propagation distance for a given offset position, which was then used as the basis for reconstruction of biomolecule holograms. The ice-embedded gold particles were also used for ice quality assessment experiments.

Precise magnitudes of phase shifts in reconstructed phase images could not be established in this study; only relative phase shifts are displayed (arbitrary units; a.u.). Furthermore, twin images in reconstructed holograms have not been removed. This will be the subject of further investigations.

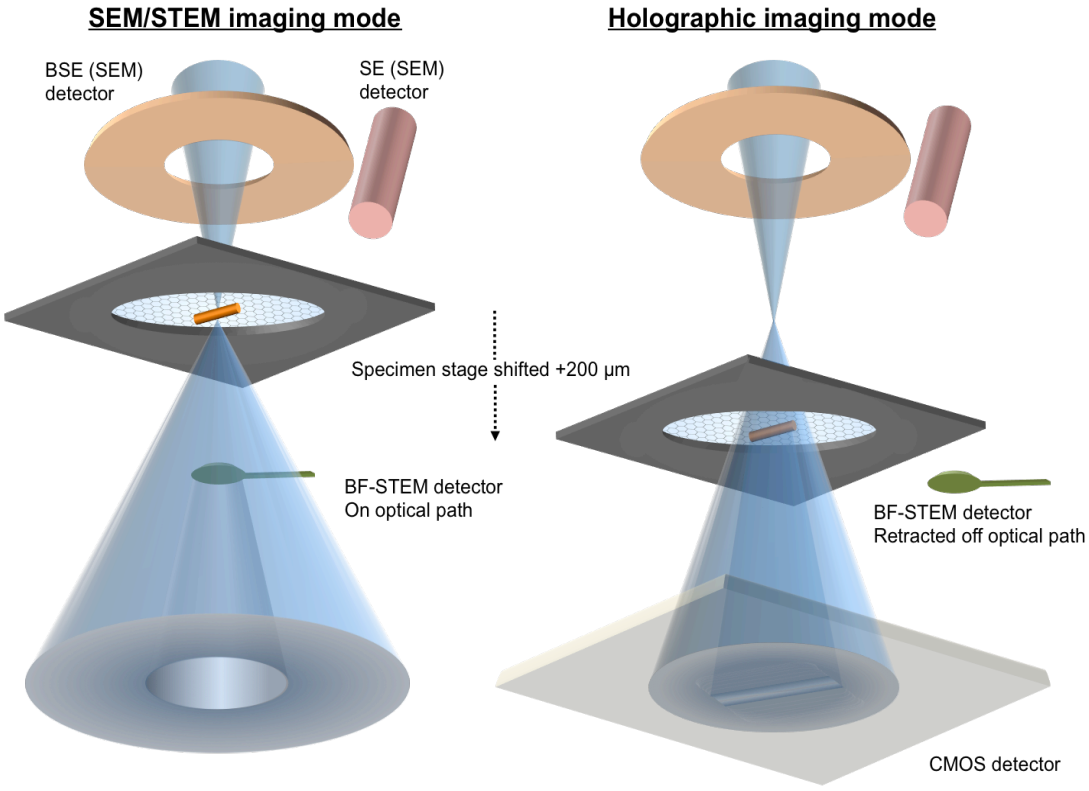

Figure 2. Transition between SEM/STEM and holographic imaging modes. Initial sample assessment is conducted using secondary electron (SE) and back-scattered electron (BSE) SEM detectors and BF-STEM detectors. Once a suitable imaging area has been identified, the incident electron beam is brought to point focus on the specimen. Transition to in-line electron holography mode is performed by retracting the BF-STEM detector off the optical beam path and shifting the specimen stage +200 µm from point focus. Electron detection is switched to a downstream CMOS detector.

Results

Seamless transition between SEM/STEM and cryo-holographic imaging modes As previously described in Adaniya et al., (2018) (4), despite its apparent complexity, imaging in DMF4000 requires little expertise above basic SEM/STEM operational competency. As is evident from figure 2, the transition between SEM/STEM and in-line holographic imaging modes can be conducted in a seamless manner, requiring no additional adjustments or modifications to pre-specimen beam optics; once requisite focus and astigmatism correction have been conducted, the specimen stage is shifted

into the divergent beam path in order to allow coherent electron waves transmitted through the ice and specimen (object wave) to interfere with those transmitted through only the ice (reference wave), resulting in an interference pattern in the near-field diffraction (Fresnel) range. The Fresnel interference pattern recorded on the detector contains not only amplitude contrast information but also phase contrast information resulting from phase variations between object and reference waves recorded in the Fresnel fringes. The extension of Fresnel fringes from the edge of the specimen and intensity of fringes above noise (i.e. “fringe contrast”) determine the contributions of phase and amplitude contrast, respectively, to the reconstructed image (17).

The implementation of holographic imaging capabilities into a commercial SEM microscope has two major benefits over conventional TEM microscopes in terms of operational ease-of-use. First, the image formation processes in SEM and STEM permit rapid wide-FOV, near-whole grid inspection. In DMF4000, the widest imageable FOV is 4,000 μm allowing for the entirety of the grid to be captured in a single, low-dose image (Figure S1a,b). Using this wide FOV, regions of the grid with areas suitable for imaging can be readily determined and logged, minimizing the time delay between sample insertion into the microscope and data acquisition. Individual grid squares are generally inspected using a 100 μm FOV, which can be achieved without altering the objective lens current since magnification is governed by scanning area and controlled by scanning coils in SEM/STEM. This greatly simplifies and expedites the transition between imaging modes (Figure S1c,d). Furthermore, the low-energy electron beam of DMF4000 enables clear visualization of contrast variations across the grid, making differences in ice thickness more apparent and perceptible than conventional TEM imaging. Utilization of the SEM/STEM functionality of DMF4000 provides a convenient and rapid means of assessing factors such as macroscopic grid contamination and ice gradation over the entire grid, which serves as useful feedback for optimizing cryo-sample preparation conditions. While cryo-TEMs can produce similarly wide FOV composite images, for example, via the semi-automated “Atlas” mode of FEI software package EPU, we have found these software-assisted

modes to be far more involved, requiring an initial beam setup step followed by a lengthy image tile acquisition and 'stitching' step. In DMF4000, a whole grid view can be acquired within minutes of commencement of the imaging session. Second, once the incident convergent beam has been focused and corrected for astigmatism, it need not be re-focused or corrected again for the duration of the holographic imaging session. When moving to a new area of the grid, variations in eucentric height along the *Z*-axis, as a result of factors such as physical grid distortions, cryo-crinkling, and ice thickness gradation can be corrected for by adjusting the stage *Z*-position so that point focus again occurs on the grid surface (i.e. eucentric focus), which can be intuitively gauged by image sharpness. Following this correction, a new *Z*=0 position is established and the stage need only be offset +200 µm from this new zero position in order to transition to holography mode. It should be noted that in holography mode, for a defined projection lens power, the offset distance of the sample determines image magnification. For example at an offset of +200 µm, the calculated effective magnification in the reconstructed image is approximately 50,000×. This can be varied from between ~33,000× and ~101,000× magnification by adjusting the offset distance to between +100 and +300 µm without any appreciable affect on achievable image resolution (at the current resolution limit of DMF4000 of approximately 2 nm). However, changes in magnification as a result of sample variations in eucentric height—typically on the nanometer scale—are imperceptible in reconstructed images and can be corrected for computationally during image reconstruction.

Cryo-SEM/STEM vs. cryo-holography All EM imaging relies on differential electron scattering (elastic and inelastic) between the specimen and surrounding medium in order to generate image contrast. In conventional single particle cryo-TEM, image contrast is generally poor owing to the low atomic mass elements (predominantly H, C, N, and O) that comprise biomolecules and water. In the energy range of 200–300 kV most small biomolecules exhibit weak inelastic scattering properties, resulting in amplitude contrast of only 6–12% in micrographs (18). In order to generate sufficient image contrast, one must measure phase shifts imparted to

elastically scattered electrons (i.e. phase contrast) by the specimen. As electron beam-energy decreases, specimens exhibit increased inelastic and elastic scattering, which are utilized in SEM and STEM via the detection of secondary (SE) and backscattered (BSE), and transmitted electrons, respectively (see figure 2 for detector configuration). While the increased scattering by the specimen could potentially lead to gains in image contrast, increased scattering by the encapsulating ice itself could negate any potential

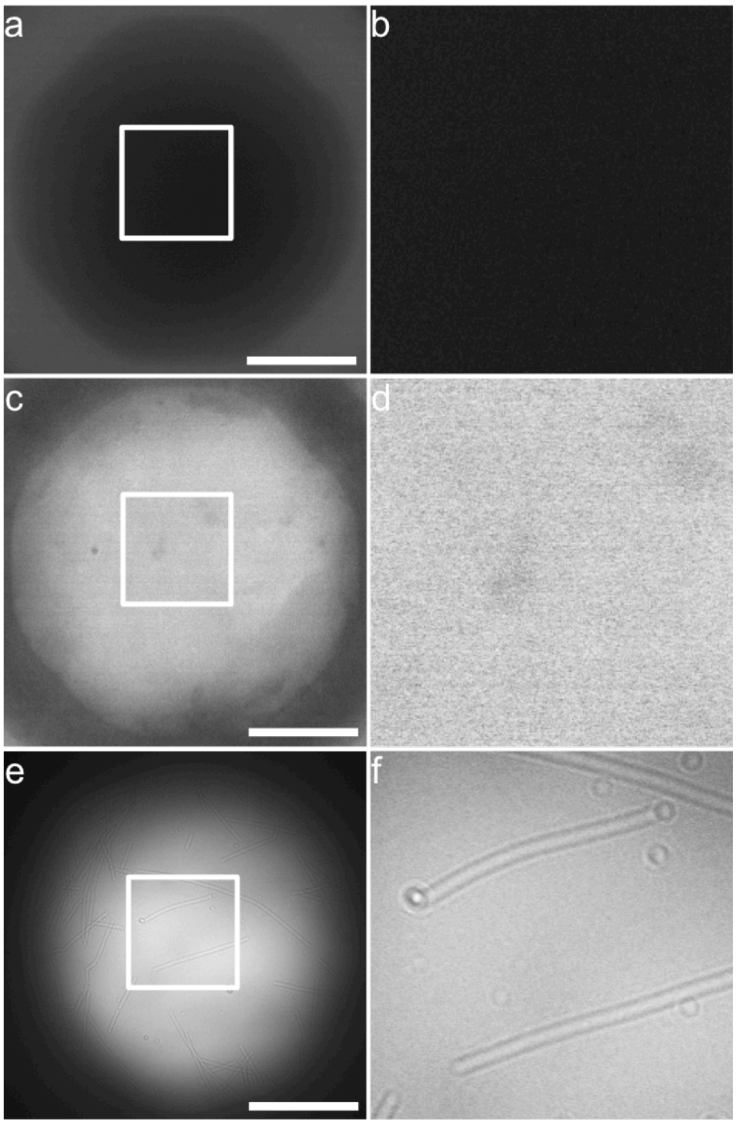

gains. To investigate whether DMF4000's SEM and STEM modalities could be applied to cryo-samples, ice-embedded tobacco mosaic virions (TMV, 18 × 300 nm in size) were visualized at 20 kV using SEM and BF-STEM detectors.

Figure 3. Low-magnification 20 kV SEM, STEM and holographic imaging of ice-embedded TMV virions. (a) SEM, **(c)** STEM, and **(e)** in-line electron holographic images of TMV virions embedded in layers of vitreous ice, spanning 3.5 µm grid holes. Each image was acquired with at an electron accelerating voltage of 20 kV. **(b,d,f)** Enlarged views of areas enclosed by white boxes in corresponding images. All scale bars, 1 µm.

As shown in figure 3, TMV virions could not be clearly discerned by either imaging mode. In the case of SEM, ice films showed low levels of SE and/or BSE detection indicating a predominance of electron transmission (Figure 3a,b). Since only scattering events that occur to a certain depth in the sample will produce detectable SE or BSE (i.e. that reach the SE and BSE detectors), SEM functions primarily as a surface imaging method at low incident beam energies (19). In the case of DMF4000, it would appear that while the majority of impinging electrons pass through the amorphous ice film, any SE and/or BSE generated by the specimen are overwhelmed by those emitted from the ice itself, the result of which are dark/near black images of the ice layer with an almost total absence of perceptible signal from the TMV virions (Figure 3b). The predominance of electron transmission is confirmed by post-sample BF-STEM detection where substantial electron detection was seen (Figure 3c,d). Despite this, however, TMV virions were not visible. BF-STEM detectors function in a binary fashion—above the energy detection threshold, either the electron is detected or not—electrons that are scattered (elastically or inelastically) but not at sufficiently high angles (e.g. <15 mrad in DMF4000) will still be recorded by the detector should they have energies above the threshold of detection. As with the SE and BSE, electrons scattered by the specimen cannot be differentiated from those scattered by the ice film. These results clearly demonstrate the main difficulty in adapting low-energy SEMs to cryo-samples; scattering by the encapsulating ice film degrades image SNR to such an extent that the sample can no longer be discriminated from background noise. Therefore, without differentiating between electrons scattered by the specimen and ice, for example through the use of differential imaging such as annular dark-field (ADF) or high-angle annular dark-field (HAADF), poor SNR will likely be an insurmountable issue in SEM and STEM.

Image formation in in-line electron holography does not suffer from the aforementioned drawbacks. Since interference between object and reference

waves mostly occurs between electrons that have retained coherency, interference and Fresnel fringe formation is primarily a function of elastic scattering (20). Through this mechanism, differences in elastic scattering cross-sections between proteinaceous compounds and vitreous ice can be exploited to differentiate between scattering by the specimen and encapsulating ice film to vastly improved image SNR and specimen contrast. The marked improvement in SNR afforded by holographic imaging is clearly evident in figure 3e,f, where multiple filamentous-shaped TMV virions are instantly discernable and overall image noise is reduced. It should also be noted that the weak coherent scattering signal from the specimen is amplified upon interference with the reference beam, further improving specimen contrast in recorded holograms (21).

Despite the superior specimen contrast afforded by cryo-holography, the utilization of electrons in holography is eminently more efficient than either SEM or STEM. For the cryo-SEM and cryo-STEM images in figures 3a–d, images were recorded with an electron probe current of ~1,000 pA over an area of 3.5 μm^2 for 1 s, resulting in a cumulative dose of ~30 $e^-/Å^2$ on the sample. In comparison, the cryo-hologram in figure 3e was captured with an electron dose rate of ~1 $e^-/A^2/s$ and an exposure time of 200 ms, resulting in a cumulative electron dose of ~0.2 $e^-/Å^2$ on the sample. Thus, superior image contrast in cryo-holography was achieved despite a ~150-fold reduction in impinging electrons on the sample. Since radiation damage can cause artefactual structural modifications, the ability to achieve improved levels of specimen contrast at lower total doses has important implications for accurate sample visualization and interpretation.

The importance of sample preparation In conventional cryo-TEM, the quality of the sample being imaged is known to dramatically impact resulting micrographs and, in turn, the attainable resolution; the “garbage in, garbage out” adage is widely upheld in the field. For this reason, endeavors that seek to improve sample preparation methods are important for the continued progress of cryo-EM (22). A decisive factor in sample preparation for cryo-TEM is the quality of the vitreous ice film. In particular, the thickness and

electron transparency of the ice encompassing the specimen have profound effects on image SNR. For DMF4000, difficulties pertaining to sample preparation are exacerbated by the low-energy incident beam and unique imaging scheme used. By operating in the energy regime of commercial low-energy SEMs, incident electrons have reduced inelastic mean free paths in ice compared with conventional cryo-TEMs, resulting in an increased number of energy-loss scattering events before and after interacting with the specimen, the effect of which is an increase in image noise and a degradation of SNR (23). In-line electron holography is particularly susceptible to energy-loss events; since inelastically scattered electrons do not contribute to Fresnel interference, concomitant with a loss of object/reference beam coherency, energy-loss events have the general effect of washing out of Fresnel fringes and amplitude dampening of the reconstructed wave (24).

In this study, we found that successful in-line electron holography in DMF4000 was strictly conditional on the ability to embed specimens in appropriately thin ice films for the specimen being imaged. In general, unsupported vitreous ice films spanning micron-wide holes of commercially available carbon-film electron microscopy grids form biconcave layers, with the thinnest ice found in regions towards the centers of grid holes. Logically, it would be highly advantageous, from the perspective for SNR and specimen contrast, to image particles localized in these regions. Unfortunately, it is the often the case, and especially so for macromolecular complexes, that specimen particles persistently and stubbornly migrate and agglomerate at the edges of holes, where ice is at its thickest (25).

For each specimen tested, we first established optimal blotting conditions, in the absence of GO, in order to generate the thinnest vitreous ice films possible, which invariably resulted in specimen particles localized at the edges of holes (Figure S2a,c,e). Then, without altering blotting conditions, hydrated-GO flakes were introduced into the workflow as per the scheme described in Cheung et al., (2018). By providing a supporting layer for specimen particles to adsorb to, particles were readily dispersed throughout the holes regardless of ice film thickness or biconcavity (Figure S2b,d,f). Vitreous ice films were estimated to be ~40-45 nm near the centers of holes

and ~90-95 nm at hole peripheries (measured by FIB milling and SEM visualization in DMF4000; data not shown). By imaging specimen particles localized towards the center of holes, sufficient coherence between object and reference waves were retained to permit Fresnel fringe formation (Figure 4a). Conversely, particles situated at the edges of holes showed very weak Fresnel interference (Figure 4b). Imaging biomolecules in suitably thin ice films proved to be a decisive factor in the successful implementation of in-line electron holography in DMF4000.

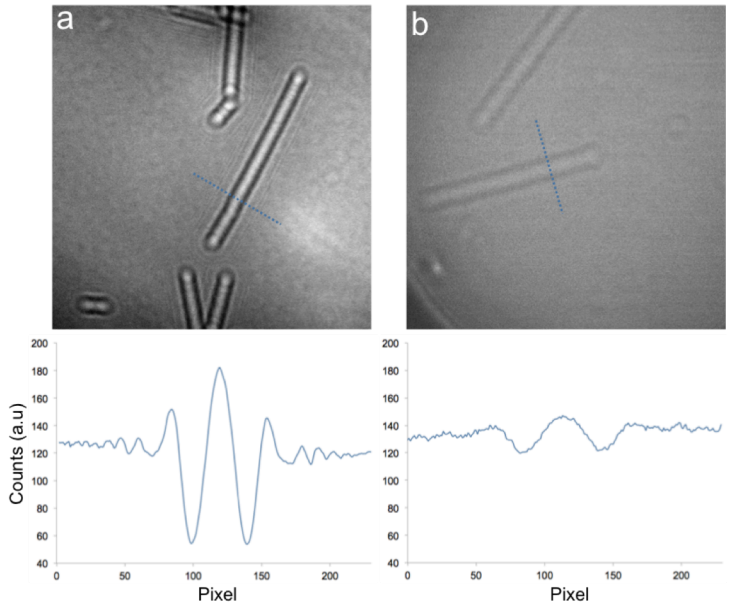

Figure 4. Effect of ice thickness on specimen contrast in in-line electron holography in DMF4000. **(a)** In-line electron hologram of TMV virions located near the center of grid hole, where ice is thinnest, displaying good Fresnel fringe contrast. Profile of detector counts along blue dotted line is shown. **(b)** In-line electron hologram and profile of detector counts for TMV virion located near edge of grid hole (edge of hole is visible in bottom left corner), where ice is thickest. Fresnel fringes display vastly reduced contrast and are virtually imperceptible.

Another factor that was found to impact specimen image contrast was the electron transparency of the vitreous ice films, a factor greatly affected by crystalline ice contamination absorbed to ice film surface. In conventional cryo-TEM, the high incident beam energies are not notably perturbed by variations in the vitreous ice film surface topography, preventing direct assessment of ice surface quality. In-line electron holography at 20 kV

allowed us to visualize phase variations, and thus quality, of ice surfaces directly. Intriguingly, we found that samples prepared in accordance with standardly used protocols exhibited vitreous ice films with significant variations in contrast, which we term ‘noisy ice’ (Figure 5a,b), likely a result of phase and/or amplitude contrast from crystalline ice contamination absorbed to the ice film surface during sample grid processing. Since the detector records the intensity of Fresnel fringes overlaid by intensity modulations of the surrounding vitreous ice, noisy ice has the effect of diminishing achievable resolution and contrast in reconstructed images. In order to reduce this effect, we established a workflow to substantially minimize noisy ice and to maximize electron transparency.

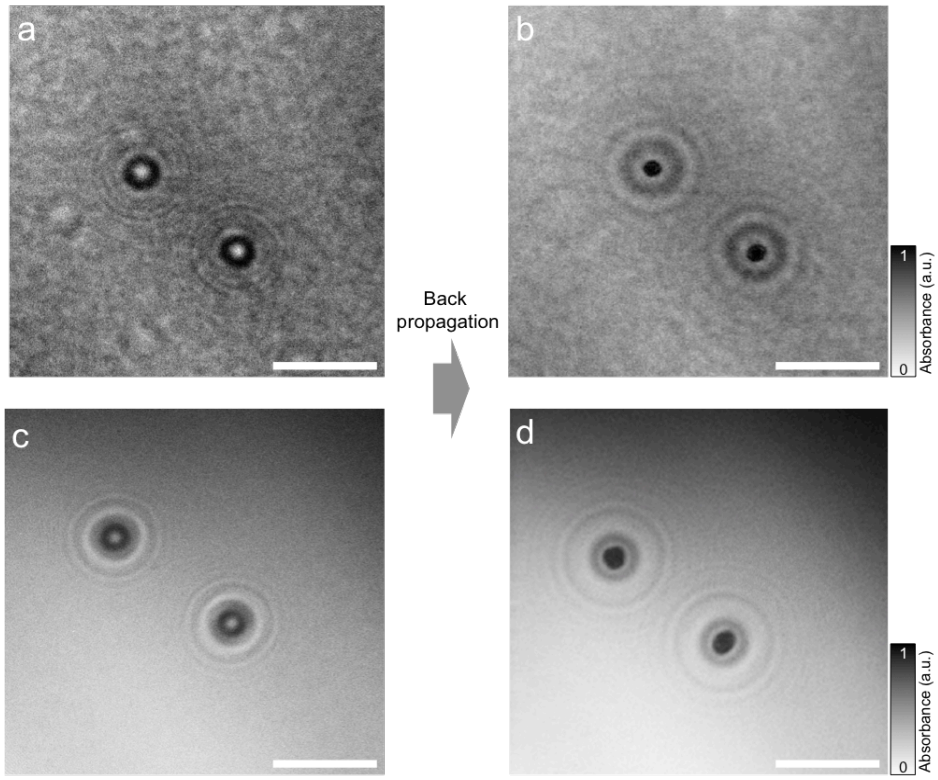

Figure 5. Optimized sample preparation reduces ‘noisy’ ice, improves transparency. (a) In-line electron hologram and **(b)** reconstructed amplitude image of ~30 nm gold particles embedded in vitreous ice, prepared by conventional sample preparation procedure. Considerable variations in contrast from region surrounding the gold particles are indicative of crystalline ice contamination adsorbed to vitreous ice layer surface. **(c)** In-line electron hologram and **(d)** reconstructed amplitude image after implementation of improved sample preparation protocols, displaying reduced noise and improved clarity of Fresnel fringes. All scale bars, 100 nm.

The central tenant of our approach was to systematically and judiciously reduce water contamination during all stages the sample preparation workflow. In particular, we found atmospheric water vapor to be a key factor in the creation of noisy ice. While it's believed that cryo-workstations prevent atmospheric water vapor contamination by establishing positive-pressure within the chamber of the cryo-workstation, preventing air and moisture from entering, we found that this to be insufficient. We optimized the sample preparation procedure by conducting the grid transfer step inside a positive-pressure chamber constantly filled with N_2, reducing ambient humidity around the cryo-workstation to below 1% (Figure S3). Along with increased attentiveness during all stages of the workflow, we greatly increased the electron transparency of vitreous ice films (Figure 5c,d). Unlike the issue of ice thickness mentioned above, noisy ice does not strictly preclude holographic imaging but instead negatively impacts resolution and contrast of reconstructed images. At the currently achievable image resolution of holography in DMF4000, these factors are not critical for successful imaging. However, as the image resolution of DMF4000 improves, the issue of electron transparency is likely to become increasingly influential.

An important consequence of the highly optimized samples was the reduced exposure times required for successful hologram formation. In practice, Fresnel fringe contrast correlates negatively with exposure time due to the washing out of interference fringes by mechanical and environmental factors. For example, excessive vibrations or drift of the sample holder during hologram acquisition will cause a loss of coherence between successive diffracted electron waves, resulting in Fresnel fringe blurring (24, 26). For such reasons, in-line electron holography benefits from minimal exposure times. As mentioned, each micrograph presented in this study was recorded with an exposure time of 200 ms. Despite the incident beam energy of 20 kV used, 200 ms exposure times at a dose rate of 1 $e^-/A^2/s$ were sufficient for successful hologram formation, acquisition and reconstruction.

High-magnification visualization of vitreous ice-embedded biomolecules by holographic imaging in DMF4000 Three morphologically distinct bio-macromolecules were selected in order to assess the in-line electron holographic imaging capabilities of DMF4000; TMV (~34 MDa), earthworm erythrocruorin (~3.6 MDa), and bacteriophage T4 (~200 MDa). These bio-macromolecules were selected due to their easily recognizable macroscopic structures at low resolutions yet fine structural features that allowed for assessment of the imaging capabilities of DMF4000.

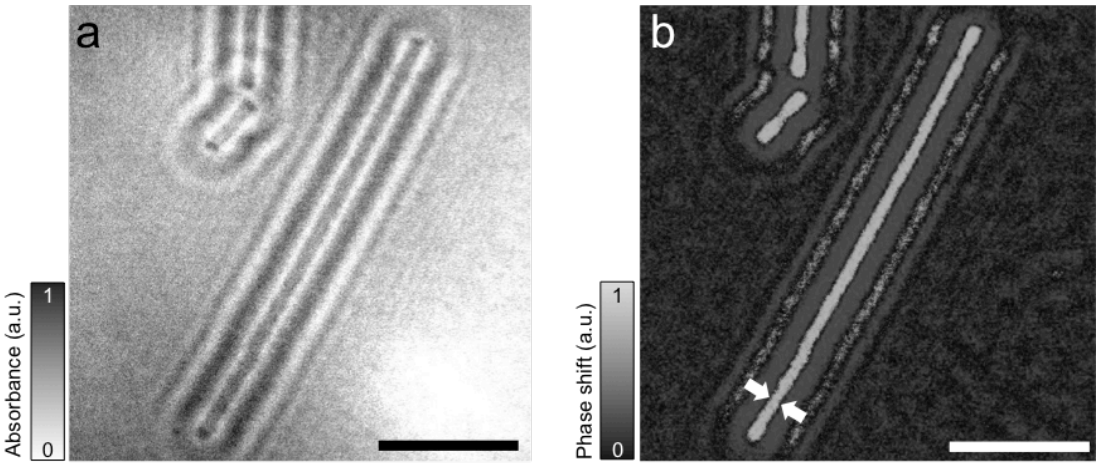

Figure 6. Reconstructed amplitude and phase images of ice-embedded TMV virions from in-line electron hologram. (a) Amplitude and **(b)** phase contrast images of ice-embedded TMV virions were reconstructed separately from an in-line electron hologram captured with an offset of +200 µm from point focus and a total dose of 0.2 $e^-/Å^2$. Block arrows indicate edge of reconstructed particle. In both cases, TMV virions display substantial contrast compared with the surrounding ice. All scale bars, 200 nm.

TMV virions are filamentous in nature, with a diameter of 18 nm and average length of 300 nm. Clear Fresnel fringes, parallel to the filament, can be seen extending from the virions (Figure 6a). In-line electron holograms recorded on the detector comprise both amplitude and phase components, with the amplitude component describing inelastically scattered electrons and those scattered out of detector range and the phase component describing phase shifts introduced to coherent electron waves by the sample (27). Phase and amplitude channels were reconstructed by computationally back propagating holograms to object plane, thereby reconstructing the wave

function of the specimen exit wave. Owing to the increased inelastic scattering cross-section afforded by the 20 kV beam used in this study, TMV virions showed considerable amplitude contrast in reconstructed images (Figure 6a). Significantly, TMV virions showed a marked increase in amplitude contrast with respect to the surrounding ice. Likewise, images reconstructed from the phase channel also displayed significant phase contrast from TMV virions, making them clearly discernable from the surrounding ice (Figure 6b). Both reconstructed images demonstrate the substantial improvements to sample preparation implemented in this study, with vastly reduced amplitude and phase variance arising from the ice.

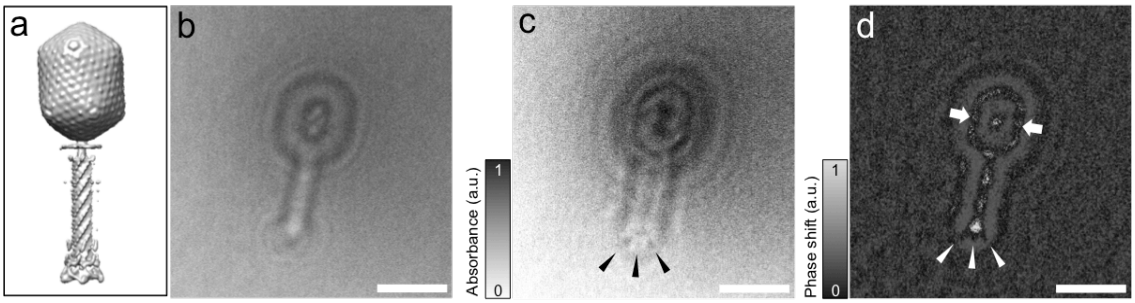

Figure 7. In-line electron hologram and reconstructed images of bacteriophage T4. (a) Electron density map of bacteriophage T4 (PDB: 2774). **(b)** Hologram of ice-embedded bacteriophage T4 virion. Reconstructed (**c**) amplitude and (**d**) phase contrast images by back propagation. Arrow heads in (c) and (d) specify clearly discernable tail-spikes. Block arrows in (d) indicate edge of reconstructed particle. Hologram was captured with an offset of +200 µm from point focus and a total dose of 0.2 $e^-/Å^2$. All scale bars, 100 nm.

Bacteriophage T4 was a particularly challenging specimen for holographic visualization owing to its unique morphology and irregular mass distribution. Comprising a large icosahedral head and filamentous tail structures, the majority of the particle's mass is concentrated in the DNA-filled head structure (~194 MDa, (28)) (Figure 7a). With a diameter of approximately 86 nm, the large head structure would typically determine the ice film thickness surrounding the particle, as it would need to be at least this thick in order to fully encompass the particle. Since the filamentous tail is considerably smaller than the head (18 nm in diameter), the ice surrounding this portion of the particle should be disproportionately thick; an ice thickness of ≥86 nm would

represent at least 68 nm of excess ice—considerably more than the thickness of the filament tail itself. As mentioned, appropriate ice thickness relative to the specimen was found to be a crucial factor for successful holographic imaging in DMF4000. It was therefore a concern that the filament tail could not be reconstructed. We found this not to be the case. Clear Fresnel fringes can be seen surrounding the filament tail portion of the T4 particle, with substantial contrast visible in reconstructed phase and amplitude images (Figure 7b–d). Furthermore, tail-spikes protruding from the baseplate on the distal end of the filament are discernable in reconstructed images (Figure 7c,d, arrow heads). Comparisons between the head and tail structures put the tail spikes at approximately 9 nm in width at the widest parts, tapering down to a few nanometers. Intriguingly, from reconstructed phase images, a negligible amount of phase contrast is lost in the filament tail. We speculate that the ice surrounding that filament tail was much thinner than estimated above. The above estimation of superfluous ice is based on the assumption of a somewhat uniformly thick ice film. However, as we previously hypothesized, the hydrated-GO process does not create a uniformly thick ice film around large macromolecules but instead creates ice films that conform to the topology of embedded particles (16). The ability to create ice films that are not substantially thicker than the embedded particles could be a crucial factor for successful in-line electron holography of irregularly shaped, large biomolecules. It should be noted that when comparing the reconstructed amplitude and phase images, visual differences are evident within the central region of the T4 head structure. Due to the voluminous nature of this structure, possibly complex internal architecture (e.g. nonuniformly distributed genome and/or accessory proteins), and limited resolution of DMF4000, it is not currently possible for us to specify the precise reason for these discrepancies.

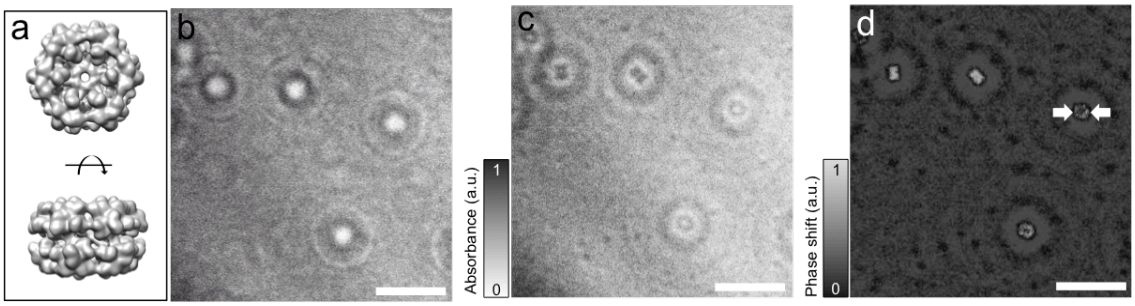

Figure 8. In-line electron hologram and reconstructed images of erythrocruorin. (a) Electron density map of erythrocruorin (PDB: 2627). **(b)** Hologram of ice-embedded **erythrocruorin**. Reconstructed (**c**) amplitude and (**d**) phase contrast images by back propagation. Block arrows in (d) indicate edge of reconstructed particle. Hologram was captured with an offset of +200 µm from point focus and a total dose of 0.2 $e^-/Å^2$. All scale bars, 100 nm.

Erythrocruorin has a significantly smaller mass and globular morphology compared with TMV and T4, with an approximate diameter of 38 nm when visualized from the top (29). Unlike TMV and T4, whose elongated structures only allow particles to adopt side-on orientations (with respect to an incident beam normal to the grid surface), erythrocruorin particles are able to adopt an array of orientations. Erythrocruorin particles with top-edge orientated towards the incident electron beam are identifiable by their C_6-rotational symmetries and central pores, distinguishing them from the more elongated morphologies of the side-on orientated particles (Figure 8a). In-line holographic imaging of ice-embedded erythrocruorin showed clear Fresnel fringes, which allowed for the successful reconstruction of amplitude and phase images (Figure 8b–d). While orthogonally orientated particles are indistinguishable in recorded holograms, side-on and top-edge orientated particles are clearly identifiable and distinguishable in both reconstructed images. At the current resolution limit of DMF4000 and with the contrast afforded by in-line holography, a qualitative assessment of ice embedded particles is possible. Interestingly, top-edge orientated particles show clear amplitude and phase differences near the centers, indicating reduced protein density in this region. While this could be attributed to the aforementioned central pore, previously published three-dimensional reconstructions of erythrocruorin suggest that the central

pore is approximately 2 nm in diameter. The current resolution limit of holographic imaging in DMF4000 is approximately 3 nm (4), which would not permit clear visualization of the central pore. Instead, we attribute this region of reduced density to a 'depression' in the erythrocruorin structure created by the inner most globin domains that surround the central pore, resulting in a 9 nm-wide region of reduced protein density.

Discussion The global SEM market stands as the most mature of all electron microscope families, with continued growth predicted over the next half decade (30). The ability to visualize ice-embedded small biomolecules by SEMs could greatly expand the accessibility and affordability of cryo-EM, widening the spectrum of compatible biomolecule targets. In this study, we have overcome a multitude of technical challenges to successfully combine the power of Dennis Gabor's holographic method with the current foremost technique in structural biology—cryo-EM.

As demonstrated by the three macromolecular biomolecules in this study, even at the current resolution limit of DMF4000, significant qualitative information about the sample can be obtained. Factors such as the presence, concentration, and dispersion of particles within the ice film can easily be determined. More intimate structural analyses are also possible with structural integrity and general overviews of tertiary/quaternary morphologies assessable. As mentioned in Adaniya et al., (2018) (4), the current optical setup of DMF4000 allows for holographic image resolution of approximately 2 nm, governed in large part by the SEM probe diameter of 2 nm (5). Decreasing the probe spot size would result in improved image resolution, a task that could be accomplished by changing the emitter in DMF4000 to a cold-field emission gun (FEG). The integration of the technology presented here into a commercial SEM that is already capable of a finer probe is also an intriguing possibility. For example, the Ultra-high Resolution SEM SU9000 developed by Hitachi Corporation (Japan) has a minimum probe diameter of 3.5 Å at 30 kV. Adapting such a microscope for in-line holographic imaging of cryo-samples could potentially deliver cryo-holograms at sub-nanometer image resolution. These and other avenues will be explored during the next

phase of development. While it remains to be seen whether the improved resolution of DMF4000 can be translated to cryo-EM studies, as it stands, the DMF4000 not only serves as a proof-of-concept—of the viability and compatibility of cryo-EM imaging in SEMs—but also a legitimate diagnostic microscope that has the potential to find use in a wide range of low-to-moderate resolution studies.

From our experience, a decisive factor in successful holographic imaging in DMF4000 was the condition of the ice film surrounding specimen particles. While sample facets such as ice film thickness, amorphous contaminants, and particle dispersion are known to greatly influence micrograph quality in conventional cryo-TEM, the unique imaging optics and high image contrast afforded by DMF4000 put increased emphasis on the assiduous optimization of such parameters. While the low-energy electron beam used in this study provided substantial technological hurdles for successful imaging, it also provided us with a unique opportunity to assess the quality of samples at an unprecedented level of detail. For example, the direct visualization of contrast variations in the amorphous ice film, resulting in noisy ice, would not be possible by conventional cryo-TEMs or SEM/STEMs. Furthermore, variations in ice thickness, both globally across the grid and within individual grid holes, and the distribution of biomolecules with the grid holes could be rapidly assessed in DMF4000. Coupled with its ease-of-use, the utility of DMF4000 as a pre-screening microscope is evident.

As has been highlighted by recent commentaries on the field and as demonstrated by projects such as SALVE III, low-energy electron microscopy is likely to play an major role in the future development of the cryo-EM field (31). This view is supported by recent findings indicting that, for a given sample thickness, the amount of useful information in electron micrographs increases with decreasing electron beam energy (32). It is our view that technologies and methodologies developed over the course of this study, both in electron optics and sample preparation, will be highly beneficial for future advancements in the cryo-EM field and other electron imaging modalities, especially as low-energy microscopes become more prominent.

Acknowledgements We would like to thank Dr. Tatsuya Asahata, Takahiro Yasuda, and Ken Kanda (Hitachi High-Tech Science Corporation, Japan) for support with DMF4000 construction and continued technical and operational advice. Our gratitude also goes to Mr. Seita Taba and Mr. Kun-Lung Li (OIST, Japan) for assistance with biomolecule purification and characterisation, and Prof. Keiichi Namba, Dr. Takayuki Kato, Dr. Tomoko Miyata, and Ms. Naoko Kajimura (Osaka University, Japan) for initial TMV samples.

This work was supported by the Okinawa Institute of Science and Technology Graduate University, Japan.

References

1. Shoemaker, S. C., and N. Ando. 2018. X-rays in the Cryo-Electron Microscopy Era: Structural Biology's Dynamic Future. *Biochemistry* 57: 277-285.
2. Vinothkumar, K. R., and R. Henderson. 2016. Single particle electron cryomicroscopy: trends, issues and future perspective. *Q Rev Biophys* 49: e13.
3. Owen, G. 2018. Purchasing an electron microscope? – Considerations and scientific strategies to help in the decision making process. *Microscopy and Analysis*
4. Adaniya, H., M. Cheung, C. Cassidy, M. Yamashita, and T. Shintake. 2018. Development of a SEM-based low-energy in-line electron holography microscope for individual particle imaging. *Ultramicroscopy* 188: 31-40.
5. Gabor, D. 1948. A new microscopic principle. *Nature* 161: 777.
6. Fink, H. W., W. Stocker, and H. Schmid. 1990. Holography with low-energy electrons. *Phys Rev Lett* 65: 1204-1206.
7. Fink, H. W., H. Schmid, H. J. Kreuzer, and A. Wierzbicki. 1991. Atomic resolution in lensless low-energy electron holography. *Phys Rev Lett* 67: 1543-1546.
8. Latychevskaia, T., J. N. Longchamp, C. Escher, and H. W. Fink. 2015. Holography and coherent diffraction with low-energy electrons: A route towards structural biology at the single molecule level. *Ultramicroscopy* 159 Pt 2: 395-402.
9. Longchamp, J. N., C. Escher, T. Latychevskaia, and H. W. Fink. 2014.

Low-energy electron holographic imaging of gold nanorods supported by ultraclean graphene. *Ultramicroscopy* 145: 80-84.
10. Longchamp, J. N., S. Rauschenbach, S. Abb, C. Escher, T. Latychevskaia, K. Kern, and H. W. Fink. 2017. Imaging proteins at the single-molecule level. *Proc Natl Acad Sci U S A* 114: 1474-1479.
11. Stevens, G. B., M. Kruger, T. Latychevskaia, P. Lindner, A. Pluckthun, and H. W. Fink. 2011. Individual filamentous phage imaged by electron holography. *Eur Biophys J* 40: 1197-1201.
12. Aoyama, K., and Q. Ru. 1996. Electron holographic observation for biological specimens: electron holography of bio-specimens. *J Microsc* 182: 177-185.
13. Dubochet, J., M. Adrian, J. J. Chang, J. C. Homo, J. Lepault, A. W. McDowall, and P. Schultz. 1988. Cryo-electron microscopy of vitrified specimens. *Q Rev Biophys* 21: 129-228.
14. Glaeser, R. M. 2013. Invited review article: Methods for imaging weak-phase objects in electron microscopy. *Rev Sci Instrum* 84: 111101.
15. Matusumoto, T., T. Tanji, and A. Tonomura. 1995. Visualization of DNA in solution by Fraunhofer in-line electron holography: II. Experiments. *Optik* 100: 71-74.
16. Cheung, M., H. Adaniya, C. Cassidy, M. Yamashita, K. L. Li, S. Taba, and T. Shintake. 2018. Improved sample dispersion in cryo-EM using “perpetually-hydrated” graphene oxide flakes. *J Struct Biol* 204: 75-79.
17. Lichte, H. 2008. Performance limits of electron holography. *Ultramicroscopy* 108: 256-262.
18. Penczek, P. A. 2010. Image restoration in cryo-electron microscopy. *Methods Enzymol* 482: 35-72.
19. Goldstein, J., D. E. Newbury, D. C. Joy, C. E. Lyman, P. Echlin, E. Lifshin, L. Sawyer, and J. R. Michael. 2003. *Scanning Electron Microscopy and X-Ray Microanalysis*. Springer Science, New York.
20. Van Dyck, D., H. Lichte, and J. C. Spence. 2000. Inelastic scattering and holography. *Ultramicroscopy* 81: 187-194.
21. Shintake, T. 2008. Possibility of single biomolecule imaging with coherent amplification of weak scattering x-ray photons. *Phys Rev E Stat Nonlin Soft Matter Phys* 78: 041906.
22. Frank, J. 2017. Advances in the field of single-particle cryo-electron microscopy over the last decade. *Nat Protoc* 12: 209-212.
23. Vulovic, M., R. B. Ravelli, L. J. van Vliet, A. J. Koster, I. Lazic, U. Lucken, H. Rullgard, O. Oktem, and B. Rieger. 2013. Image formation modeling in cryo-electron microscopy. *J Struct Biol* 183: 19-32.
24. Lichte, H. 2013. Electron Holography: phases matter. *Microscopy (Oxf)* 62 Suppl 1: S17-28.
25. Burrows, N. D., and R. L. Penn. 2013. Cryogenic transmission electron microscopy: aqueous suspensions of nanoscale objects. *Microsc Microanal* 19: 1542-1553.
26. Latychevskaia, T., and H. W. Fink. 2017. Resolution enhancement in in-line holography by numerical compensation of vibrations. *Opt Express* 25: 20109-20124.
27. Latychevskaia, T., and H. W. Fink. 2009. Simultaneous reconstruction of phase and amplitude contrast from a single holographic record. *Opt Express* 17: 10697-10705.

28. Fokine, A., P. R. Chipman, P. G. Leiman, V. V. Mesyanzhinov, V. B. Rao, and M. G. Rossmann. 2004. Molecular architecture of the prolate head of bacteriophage T4. *Proc Natl Acad Sci U S A* 101: 6003-6008.
29. Chen, W. T., Y. C. Chen, H. H. Liou, and C. Y. Chao. 2015. Structural basis for cooperative oxygen binding and bracelet-assisted assembly of Lumbricus terrestris hemoglobin. *Sci Rep* 5: 9494.
30. Consultants, W. R. 2019. Global Scanning Electron Microscopy (SEM) Market Status and Future Forecast 2015-2024d.
31. Linck, M., P. Hartel, S. Uhlemann, F. Kahl, H. Muller, J. Zach, M. Haider, M. Niestadt, M. Bischoff, J. Biskupek, Z. Lee, T. Lehnert, F. Borrnert, H. Rose, and U. Kaiser. 2016. Chromatic Aberration Correction for Atomic Resolution TEM Imaging from 20 to 80 kV. *Phys Rev Lett* 117: 076101.
32. Peet, M. J., R. Henderson, and C. J. Russo. 2019. The energy dependence of contrast and damage in electron cryomicroscopy of biological molecules. *Ultramicroscopy*

Supplementary materials

Biomolecule purification protocols

Tobacco mosaic virus 5 mg of dried *Nicotiana tabacum* leaves infected with tobacco mosaic virus (TMV) were homogenized in 500 µl of 0.05 M phosphate buffer pH 7.2 using a BioMasher-II cell homogenizer (Nippi Inc.). Cell debris was removed by centrifugation at 15,000 ***g*** for 10 min at 4 °C and cell extract, containing TMV virions, collected. TMV virions were harvested by high-speed centrifugation at 55,000 ***g*** for 1 hr at 4 °C. Pelleted TMV virions were resuspended in 50 µl of Milli-Q water.

To remove membrane-bound organelle contaminants, 5 µl of 5% Triton X-100 (Sigma Aldrich) was added to the sample and incubated for 5 min. The mixture was dialyzed overnight against 500 ml Milli-Q water using a 0.5 ml Slide-A-Lyzer MINI Dialysis Device with a 20,000 Da molecular weight cutoff (Thermo Fisher Scientific). The dialyzed sample was transferred to a 1.5 ml microfuge tube, sample volume increased to 1 ml with distilled water and centrifuged at 30, 000 ***g*** for 1 hr at 4 °C to harvest the TMV virions. The resulting pellet was resuspended in 50 µl Milli-Q water.

Erythrocruorin purification from earthworm *Lumbricus terrestris* Prior to blood extraction, earthworms were left in Milli-Q water for at least a day in order to allow for excretion of internal waste. Earthworms were cleaned with Milli-Q water to remove the external mucus membrane and dried with tissue. Using a sharp scalpel, earthworms were cut just behind the cerebral ganglia. Blood was collected using a syringe with a 22 gauge needle and expelled into a 1.5 ml microcentrifuge tube. The volume of the collected fluid was increased to 1 ml with 100 mM Tris-HCl pH 7.0, 1 mM EDTA. Cell debris and particulate contaminants were pelleted by centrifugation at 20,000 ***g*** for 20 min at 4 °C. The supernatant was collected and the centrifugation step repeated. Following the second centrifugation step, the supernatant was collected and erythrocruorin pelleted by centrifugation at 150,000 ***g*** for 2 hr at 4 °C. The resulting pellet was resuspended in 1 ml of 100 mM Tris-HCl pH 7.0, 1 mM EDTA and the centrifugation step repeated. Pelleted erythrocruorin particles were resuspended in 50 µl of 100 mM Tris-HCl pH 7.0, 1 mM EDTA.

Enterobacteriophage T4 purification 3 ml of growth buffer 702 (10 g polypepton, 20 g yeast extract, 1 g $MgSO_4.7H_2O$ in 1L Milli-Q water, pH 7.0) was inoculated with *E. coli* (NBRC 13168) and incubated overnight at 30 °C. The following day, 3 ml of 702 was inoculated with 300 µl of overnight culture and incubated for 4 hr at 30 °C. 313 µl of culture was mixed with 5 ml of top-agar (10 g polypepton, 20 g yeast extract, 1 g $MgSO_4.7H_2O$, 6 g agar in 1L Milli-Q water, pH 7.0), which had been kept at 45 °C, and a diluted solution of enterobacteriophage T4. The mixture was poured onto the surface of 802 agar (10 g polypepton, 20 g yeast extract, 1 g $MgSO_4.7H_2O$, 15 g agar in 1L Milli-Q water, pH 7.0) in an agar plate and allowed to set. Ten of these plates were prepared and allowed to incubate overnight at 37 °C. Following incubation, the multiplication of T4 was confirmed by the appearance of ‘halos’ in the top-agar. Top-agar containing T4 was scraped off with a spatula and placed into a 50 ml centrifuge tube and centrifuged at 9,100 ***g*** for 15 min at 4 °C. The supernatant was collected and filtered (PALL Acrodic 0.8/0.2 µm) to obtain T4 virions.

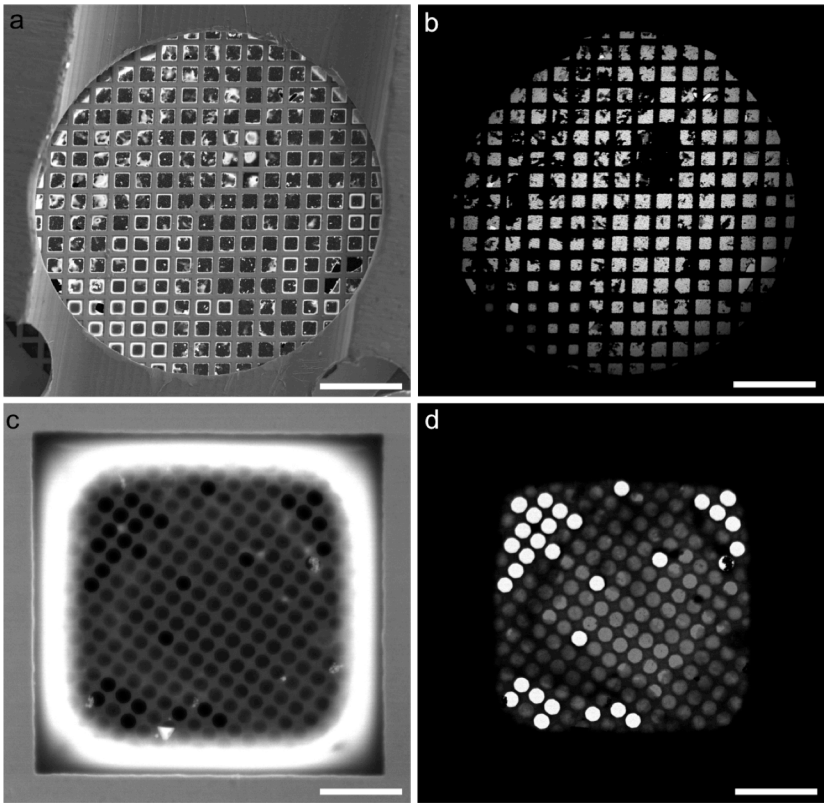

Figure S1. Single-shot whole grid and grid square inspection of vitrified sample on R3.5/1 Au 200 mesh grid using SEM and STEM imaging modes. (a) SEM and **(b)** STEM micrographs of cryo-sample captured using 4,000 µm field-of-view. Images were captured directly after insertion into the microscope column, allowing for immediate assessment of sample quality. **(c,d)** Once candidate squares were identified, 100 µm field-of-view images were captured to identify suitable holes for imaging. Scale bars, 600 µm in a,b; 20 µm in c,d.

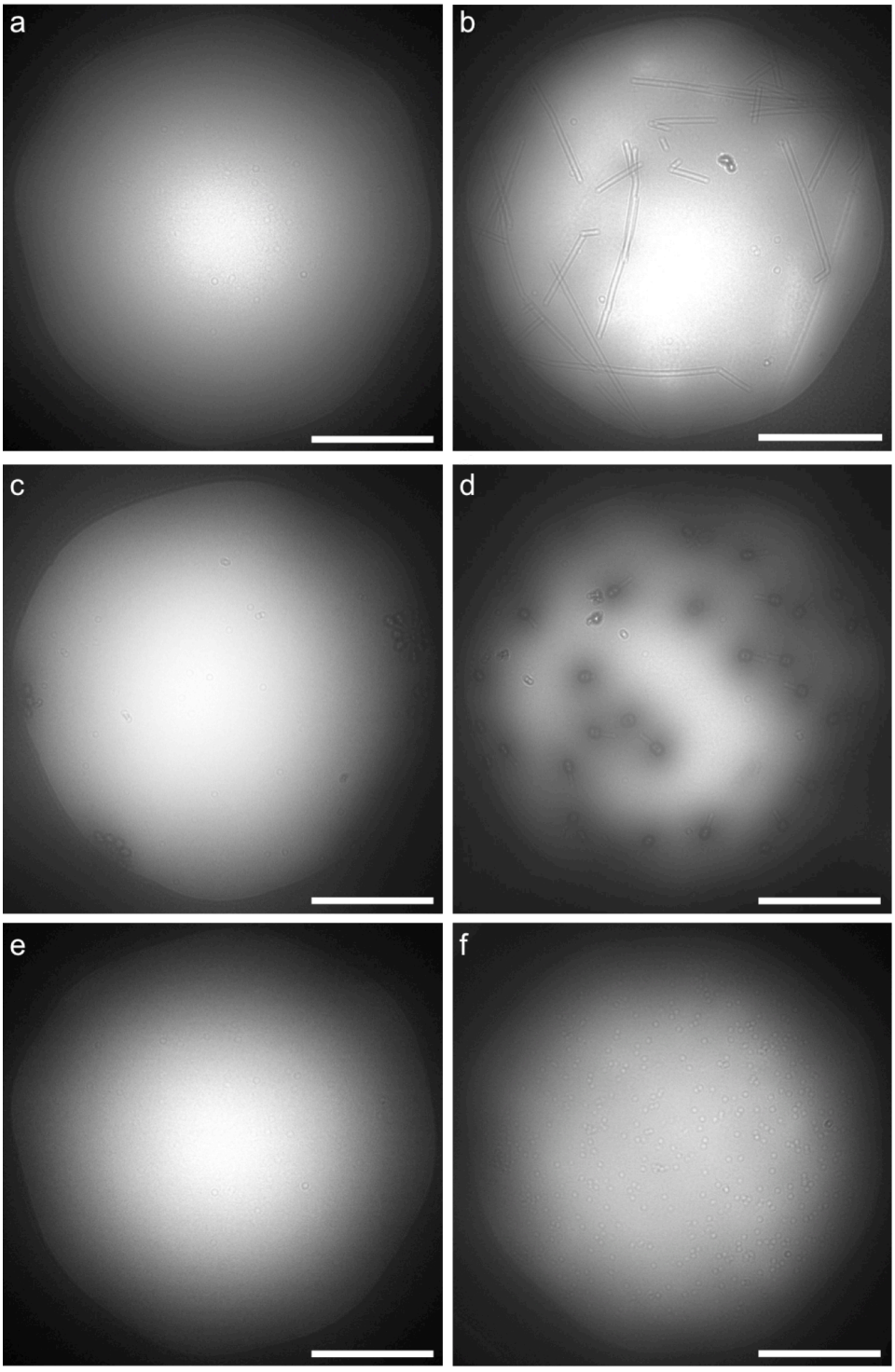

Figure S2. In-line electron holograms of grid holes containing ice-embedded biomolecules, before and after graphene oxide optimization. TMV cryo-sample prepared **(a)** without and **(b)** with the use of graphene oxide showing improved particle dispersion and density towards the center of the grid hole. Equivalent images of bacteriophage T4 **(c,d)** and erythrocruorin **(e,f)**. All scale bars, 1,000 µm. For more information see Cheung et al., 2018.

Figure S3. Cryo-sample preparation room situated at the Okinawa Institute of Science and Technology, Japan. All cryo-samples in this study were prepared in a dedicated preparation room to minimize moisture contamination. Before commencing sample preparation, the room was dehumidified to ~30% humidity. Sample grids were prepared by the plunge-freezing method in a semi-automated fashion with the FEI Mark IV Vitrobot (right) before immediate transfer to an N_2-filled, positive-pressure glove box (left) located directly beside the Vitrobot. Humidity within the glove box was kept below 1% at all times. Transfer of the sample grid into the cryo-workstation and holder were conducted within the glove box, vastly reducing visible crystalline ice contamination, resulting in significant improvements in vitreous ice transparency (16).